Rare Metal Materials and Engineering
Volume 55, Issue 3, March 2026
Available online at www.rmme.ac.cn

Science Press

Cite this article as: Wang Xu, Dang Qian, Ma Hongyao, et al. Effects of Element Y on Grain Refinement and Mechanical Properties of Cast Al-2.2Li-1.5Cu-Based Alloy[J]. Rare Metal Materials and Engineering, 2026, 55(03): 602-614. DOI: https://doi.org/10.12442/j.issn.1002-185X.20250152.

ARTICLE

Effects of Element Y on Grain Refinement and Mechanical Properties of Cast Al-2.2Li-1.5Cu-Based Alloy

Wang Xu[1], Dang Qian[1], Ma Hongyao[1], Liu Guohuai[1], Zhang Chi[2], Wang Zhaodong[1,3]

[1] State Key Laboratory of Digital Steel, Northeastern University, Shenyang 110819, China; [2] School of Materials Science and Engineering, Shenyang University of Technology, Shenyang 110870, China; [3] Institute of Materials, Henan Academy of Sciences, Zhengzhou 450046, China

Abstract: The effect of trace addition of 0.1wt% Y on the grain refinement and mechanical properties of Al-2.2Li-1.5Cu-0.5Mg-1Zn-0.2Zr-0.2Sc alloys at as-cast and heat-treated states was investigated. Results show that the addition of 0.1wt% Y into the Al-2.2Li-1.5Cu-0.5Mg-1Zn-0.2Zr-0.2Sc alloys can elevate the nucleation temperature of the Al_3(Sc, Zr) phase, leading to the preferential precipitation of the Al_3(Sc, Zr) phase and increasing the amount of Al_3(Sc, Zr) phase in the matrix. Al_3(Sc, Zr) phase can also act as a heterogeneous nucleation site in the α-Al matrix to promote nucleation and refine grains. The addition of element Y changes the precipitation phase characteristics at the grain boundaries in the as-cast alloy, which changes the distribution characteristics of secondary phases from initially continuous and coarse strip-like distribution at grain boundaries into the discontinuous dot-like and rod-like distribution. Besides, the size of secondary phases becomes smaller and their amount increases. Under the combined effects of grain refinement strengthening and precipitation strengthening, the Al-2.2Li-1.5Cu-0.5Mg-1Zn-0.2Zr-0.2Sc-0.1Y alloy after 175 °C/10 h aging treatment achieves an ultimate tensile strength of 412 MPa and an elongation of 6.3%. Compared with those of the alloy without Y addition, the ultimate tensile strength and elongation of the added alloy increase by 16.1% and 53.7%, respectively.

Key words: Al-Li alloy; element Y; heat treatment; grain refinement

1 Introduction

Aluminum-lithium alloys with low density, high stiffness, high damage tolerance, and good resistance against stress corrosion cracking can better meet the growing demand for high-performance structural materials in the aircraft, aerospace, and defense industries[1–5]. Lithium is the lightest metal[6–7] with the density of 0.534 g/cm^3. Ref.[8] reported that the addition of every 1wt% Li into aluminum alloys can reduce the density by 3% and increase the Young's modulus by 6%, thus leading to mass reduction and stiffness enhancement[9–10]. As-cast aluminum-lithium alloy has higher lithium content, lower density, and excellent fluidity. The casting performance is very competitive and can well meet the preparation requirements of large and complex structural parts[11]. In addition, the low-cost casting process can produce structurally complex components while effectively avoiding anisotropy in deformed aluminum-lithium alloys. However, for the current casting of aluminum-lithium alloys, the biggest problem is the microstructure and segregation of coarse grains, which will greatly affect the mechanical properties of alloys. Therefore, the application of aluminum-lithium alloys is seriously restricted. Overcoming this challenge for the further development of aluminum-lithium alloys is essential[2].

Aluminum-lithium alloys used as aerospace materials require both high strength and high toughness. By adding trace alloying elements, such as Sc and Zr, the grains of the alloys can be effectively refined to achieve the purpose of enhancement in strength and plasticity[12–13]. Generally, the microalloying effect has two manifestations: (1) the precipitation of strengthening phase by reducing the solubility

Received date: March 24, 2025
Foundation item: National Natural Science Foundation of China (52071065); Fundamental Research Funds for the Central Universities (N2007007); Joint Fund of Henan Province Science and Technology R&D Program (N225200810040); High-Level Talent Research Start-Up Project Funding of Henan Academy of Sciences (N242017003); Liaoning Provincial Department of Education Basic Research Projects for Colleges and Universities (LJ212410142093)
Corresponding author: Liu Guohuai, Ph. D., Professor, State Key Laboratory of Digital Steel, Northeastern University, Shenyang 110819, P. R. China, Tel: 0086-24-83673883, E-mail: liugh@ral.neu.edu.cn

of precipitated components in the matrix; (2) the formation of a new strengthening phase[14]. It is found that the addition of Sc, Zr, and other elements will promote the precipitation of Al_3Sc and $Al_3(Sc, Zr)$ phases, which have a co-lattice relationship with the matrix and can serve as heterogeneous nucleation sites, therefore promoting the nucleation and significantly refining the alloy grains. Wang et al[15] investigated the effects of combined addition of Sc and Zr on the microstructure and mechanical properties of Al-Li-Cu alloys. The results showed that Sc and Zr had a significant effect on the grain refinement of the alloy, and the addition of Sc and Zr promoted the transformation from original coarse dendritic microstructure into equiaxed crystals. The main reason for the grain refinement is that the $Al_3(Sc, Zr)$ orientation of primary grains is similar to that of the α-Al matrix, which prevents the inappropriate diffusion of α-Al during solidification. Additionally, the $Al_3(Sc, Zr)$ phase becomes a heterogeneous nucleation site for α-Al, thus promoting the grain refinement. Zhang et al[16] investigated the effect of Sc addition on the microstructure and mechanical properties of as-cast Al-2Li-2Cu-0.2Zr alloy after thermal exposure. A small amount of Sc addition significantly increased the precipitation of $Al_3(Li, Sc, Zr)$ phase, which led to a significant increase in plasticity. The addition of Sc promoted the precipitation of finer θ''/θ' phases, which was the main reason for the strength enhancement. Zhang et al[17] investigated the effect of Sc addition on the microstructure evolution and high-temperature mechanical properties of Al-Li-Cu-Mg alloys. The results showed that the addition of 0.2wt% Sc significantly increased the precipitation density of core/shell $Al_3(M, Zr, Li)$ composite particles and promoted the precipitation of plate-like S/S′ phases during aging treatment. At 200 °C or lower temperature, the superior mechanical properties of Sc-containing alloys are primarily attributed to the combined effects of multiple mechanisms, including dislocation shearing (δ'-Al_3Li) and Orowan strengthening (core/shell $Al_3(M, Zr, Li)$ composite particles).

To further refine the grains in alloys, the effect of Y addition on the microstructure and properties of aluminum alloys has been investigated. The results showed that the addition of trace Y can effectively refine the grains in alloy and significantly improve the mechanical properties of the alloy. Zhang et al[18] investigated the effects of Y contents on the microstructure and mechanical properties of Al-Zr alloys. A small amount of Y addition can effectively refine the grains of Al-Zr alloys, and the mechanical properties of Al-Zr alloys are improved with the increase in Y content. However, excessive Y addition is detrimental to the recrystallization resistance of Al-Zr alloys, which reduces the mechanical properties of the alloys. Li et al[19] investigated the effect of Y content on the precipitation hardening and mechanical properties of 2519 aluminum alloy. The results showed that the addition of 0.1wt% Y led to the precipitation of the thermally stable intermetallic compound AlCuY in the alloy, while also promoted the extensive precipitation of the δ' strengthening phase, thereby enhancing the strength of 2519 aluminum alloy.

Currently, there are few studies on the effects of the rare earth Y addition on the microstructure and mechanical properties of Al-Li alloys, and the mechanism of the Y addition effect in aluminum-lithium alloys has not yet been clearly elucidated. In this research, Y was chosen as the research object. Through thermodynamic simulation calculations and microstructure characterization analysis, the effects of Y addition on the quantity and size of various strengthening precipitates in Al-2.2Li-1.5Cu-0.5Mg-1Zn-0.2Zr-0.2Sc alloys were investigated, as well as the grain refinement mechanism contributing to the enhancement of mechanical properties[20]. This research provides theoretical basis for the feasibility of adding Y to aluminum-lithium alloys for the enhancement in their mechanical properties.

2 Experiment

The initial raw materials for the preparation of Al-2.2Li-1.5Cu-0.5Mg-1Zn-0.2Zr-0.2Sc and Al-2.2Li-1.5Cu-0.5Mg-1Zn-0.2Zr-0.2Sc-0.1Y alloys in this study were industrial pure Al (99.99%), pure Mg (99.99%), pure Zn (99.99%), Al-50Cu, Al-10Li, Al-2Sc, Al-5Zr, and Mg-30Y master alloys. The prepared alloys without and with the addition of 0.1wt% Y were denoted as Base alloy and 0.1Y alloy, respectively. Vacuum centrifugal casting was used to melt and prepare the casting rings of Base alloy and 0.1Y alloy. The melting crucible was made of a high-purity graphite crucible, and the inner part of the crucible was evenly coated with boron nitride paint to prevent the crucible from being damaged by the reaction between graphite and high-temperature alloy melt during the melting process. Specific melting steps were as follows. (1) Fix the high-purity graphite crucible coated with boron nitride inside the heating coil device. Place pure aluminum, Al-10Li master alloy, and other minor master alloys into the crucible in sequence, and then close the furnace lid. (2) Turn on the mechanical pump to initiate pre-vacuum pumping. When the furnace pressure reached 1000 Pa, activate the root pump for fine pumping until the pressure dropped to 200 Pa. After reaching the ideal vacuum condition, stop the vacuum pumping. (3) Open the argon filling valve to introduce argon gas into the vacuum centrifugal induction melting furnace. Close the argon valve after reaching a certain pressure. (4) Turn on the circulating water system and the high-frequency induction heating control cabinet. Supply power was 20 kW, and the holding time was 5 min to preheat the crucible. Then, increase the supply power to 50 kW for rapid heating. When the molten metal appeared at the crucible bottom, reduce the supply power to 25 kW, allowing the residual heat in the crucible and the exothermic reactions of the metals to fully melt the remaining material. (5) After the metal in the crucible was completely melted, the centrifugal turntable was opened, and the centrifugal speed was set as 800 r/min. Hold the molten metal temperature at 750 °C for 10 min. Subsequently, the metal was poured into a uniformly rotating metal mold at 750 °C. Open the furnace, and remove the alloy ingot when the alloy was cooled to room temperature

in the furnace.

The as-cast Base and 0.1Y alloys were subjected to a continuous two-stage homogenization treatment (480 °C/5 h+ 530 °C/5 h), followed by water quenching at room temperature to obtain a supersaturated solid solution. Tensile specimens and cubes of 10 mm×10 mm×2 mm for microstructure observation were cut from the outside of the cast ring. Subsequent artificial aging was performed at 175 °C for 8, 10, and 14 h to promote the precipitation of the δ' (Al_3Li) main strengthening phase and some Cu-rich nanoscale strengthening phases.

Sequentially, use 600#, 800#, 1000#, 1500#, 2000#, and 3000# SiC sandpapers to grind the specimen surface until no obvious scratches were visible. After the specimens were mechanically polished with magnesium oxide polishing solution at 900 r/min to reach the mirror-like state, chemical corrosion was conducted using Keller's reagent (2.5 mL HNO_3+1.5 mL HCL+1 mL HF+95 mL H_2O) for about 15 s. Microstructure and phase composition analyses were conducted using optical microscope (Imager M2m ZEISS), field emission scanning electron microscope (SEM, ZEISS-ULTRA-55), and field emission electron probe microanalyzer (JEOL JXA-8530F). The specific contents of each chemical element in the alloys were analyzed and measured using inductively coupled plasma-atomic emission spectroscope (ICP-AES), and the results are shown in Table 1. The average grain size in the specimens was quantitatively analyzed using Image-Pro-Plus image software. The phase composition of the alloys was analyzed using energy dispersive spectrometer (EDS) and X-ray diffractometer (XRD) with a copper target (scanning angle of 10°–90°; scanning speed of 4°/min). Room-temperature tensile tests were conducted on the heat-treated Base and 0.1Y alloys using a universal tensile testing machine at strain rate of 0.2 mm/min. The final tensile properties were determined by averaging the results of three tensile specimens to ensure the experiment accuracy. The dimensions of the tensile specimens are shown in Fig.1. The gauge length was 25 mm, the width was 6 mm, and the thickness was 2 mm. The fracture morphologies of the tensile specimens was observed by SEM to analyze the fracture mechanism. Transmission electron microscope (TEM) was used for analysis, as well as selected area electron diffraction (SAED) pattern.

3 Results

3.1 Microstructure and phase analysis of as-cast alloys

Fig. 2a – 2b show the microstructures of Base alloy. According to Fig. 2a, the alloy microstructure is uniformly dense without obvious defects, and the grain morphology consists of regular equiaxed grains without the presence of

Table 1 Actual element contents in Base and 0.1Y alloys measured by ICP-AES (wt%)

Alloy	Li	Cu	Mg	Zn	Zr	Sc	Y	Al
Base	2.230	1.470	0.453	0.974	0.215	0.157	-	Bal.
0.1Y	2.180	1.430	0.452	0.893	0.207	0.163	0.087	Bal.

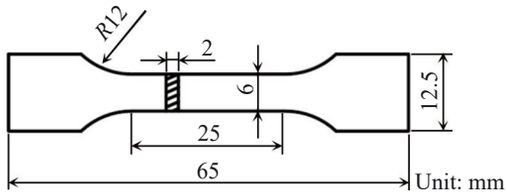

Fig.1 Schematic diagram of tensile specimen

coarse columnar grains. The microstructure consists of an α-Al matrix, cubic phases precipitated within the grains, and a large number of strip-like secondary phases precipitated along the grain boundaries, as shown in Fig.2b and 2e. Fig.2d–2e show the microstructures of 0.1Y alloy. Compared with that of the Base alloy, the microstructure of 0.1Y alloy also consists of an α-Al matrix, cubic phases precipitated within the grains, and secondary phases precipitated along the grain boundaries. The difference is that the 0.1Y alloy has finer grains, more cubic phases within the grains, and more secondary phases at the grain boundaries. According to Fig. 2b, the microstructure exhibits distinct wide grain boundary characteristics, which may indicate some degree of element segregation during the solidification process. The grain sizes of the two alloys are shown in Fig.2c and 2f. The average grain sizes of the as-cast Base and 0.1Y alloys are 29.81 and 18.56 μm, respectively.

Fig.3 shows the phase composition of the as-cast Base and 0.1Y alloys. The results indicate that both alloys consist of δ (AlLi) phase, δ' (Al_3Li) phase, T_1 (Al_2CuLi) phase, S′ (Al_2CuMg) phase, β' (Al_3Zr) phase, Al_3Sc phase, and T_2 (Al_6CuLi_3) phase. The Y-containing secondary phase cannot be detected in the 0.1Y alloy, probably because it is slightly added and mostly melted into the matrix.

The non-equilibrium solidification paths of the Base alloy and 0.1Y alloy were calculated using the thermodynamic simulation software Jmatpro[21]. As shown in Fig. 4a, in the Base alloy, the Al_3Zr phase is precipitated firstly from the liquid phase when the temperature decreases. With the cooling further proceeding, the Al_3Sc phase, α-Al phase, T_2 (Al_6CuLi_3) phase, T_1 (Al_2CuLi) phase, and S′ (Al_2CuMg) phase are precipitated sequentially. The solidification paths of the precipitated phases are basically the same for both alloys, as shown in Fig. 4. The difference is that the addition of Y increases the initial precipitation temperatures of the Al_3Zr and Al_3Sc phases. In the 0.1Y alloy, the precipitation temperatures of Al_3Zr and Al_3Sc phases are 815 and 726 °C, which increase by 15 and 12 °C compared with those of the Base alloy, respectively. This phenomenon results in the preferential precipitation of these two phases in the 0.1Y alloy, leading to higher contents of these two phases in the matrix.

Fig.5a and 5d show SEM microstructures of Base and 0.1Y alloys. It is observed that the number of secondary phases in the 0.1Y alloy is significantly larger than that in the Base alloy, and the grain size is also finer. The area fractions of secondary phase are quantified using Image-Pro-Plus software, and the specific results are shown in Fig.5a and 5d.

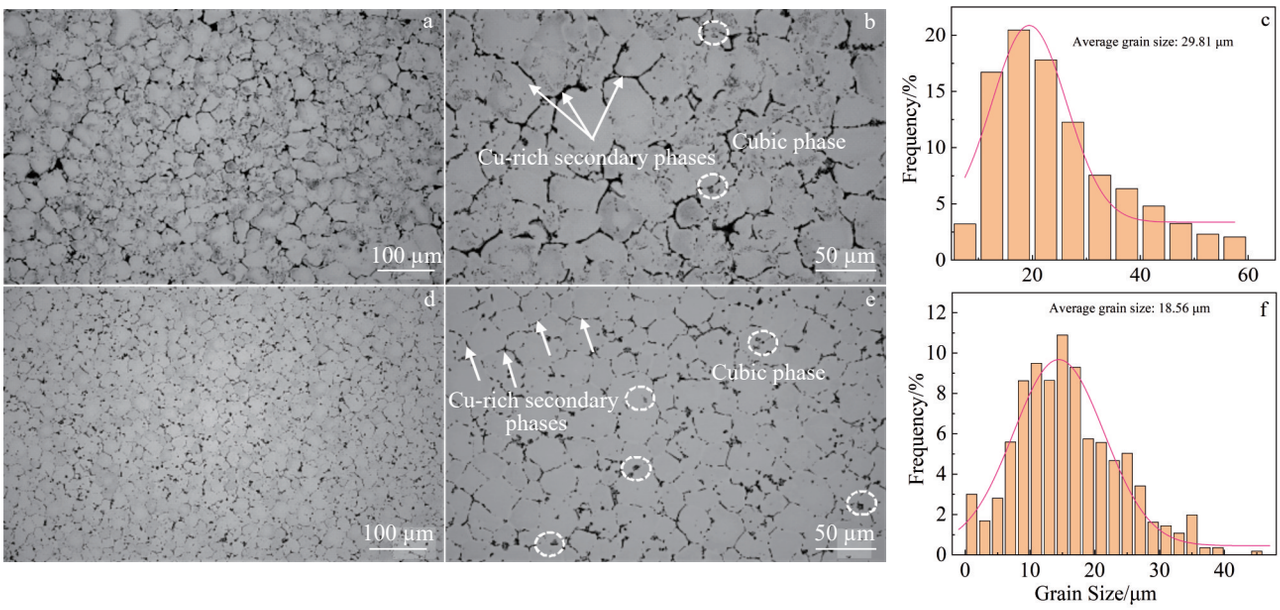

Fig.2 Microstructures (a–b, d–e) and grain size distributions (c, f) of as-cast Base alloy (a–c) and 0.1Y alloy (d–f)

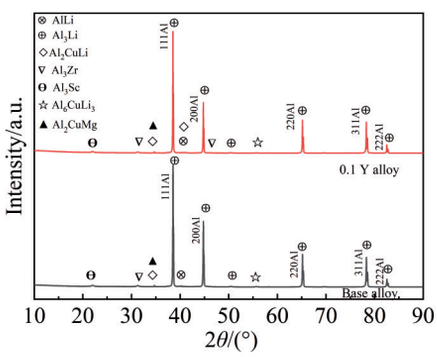

Fig.3 XRD patterns of as-cast Base and 0.1Y alloys

The area fraction of secondary phase is 3.524% and 4.633% in the Base alloy and 0.1Y alloy, respectively. Fig.5b and 5e also show that the precipitates at the grain boundaries of both alloys are mainly distributed in a continuous strip-like pattern, whereas the precipitates inside the grains exhibit a discrete distribution of blocky and rhombic shapes. The specific composition of the precipitates at the grain boundaries and within the grains was analyzed, and the results are shown in Table 2. The precipitate phases at the grain boundaries are mainly Cu-rich secondary phases. Based on the detected atomic ratios of Al and Cu, it can be determined that the precipitates at grain boundary in the Base alloy are primarily mixed phases, such as T_2 (Al_6CuLi_3) and T_1 (Al_2CuLi) phases. In the 0.1Y alloy, Y-containing Cu-rich secondary phases are also detected at the grain boundaries, as shown in Fig. 5f. Based on Ref. [22], it is speculated that these phases may be Al_8Cu_4Y. The cubic block-shaped precipitates within the grains of both alloys, as shown in Fig.5c, are primary $Al_3(Sc, Zr)$ phases formed during solidification. It is generally recognized as a common phase with high thermal stability in Al alloys co-added with Sc and Zr.

Fig.6 shows SEM images and corresponding EDS element distributions of as-cast Base and 0.1Y alloys. According to Fig. 6b, the element Zn in the Base alloy is uniformly distributed throughout the microstructure. Most of the Cu is polarized and precipitated at the grain boundaries to form a Cu-rich secondary phase, such as Al_2CuLi and Al_6CuLi_3. The

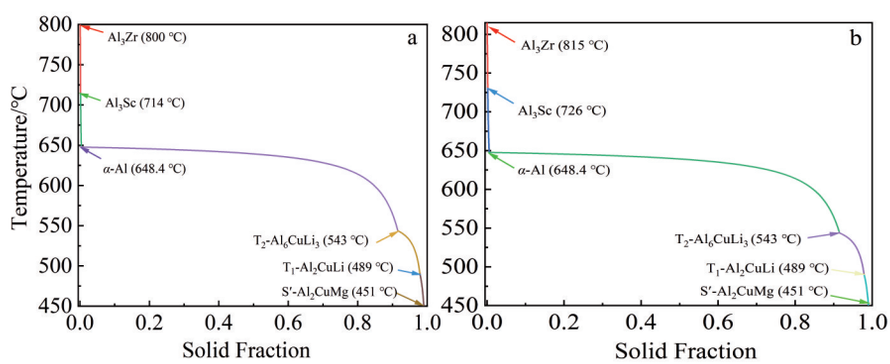

Fig.4 Non-equilibrium solidification paths for Base alloy (a) and 0.1Y alloy (b)

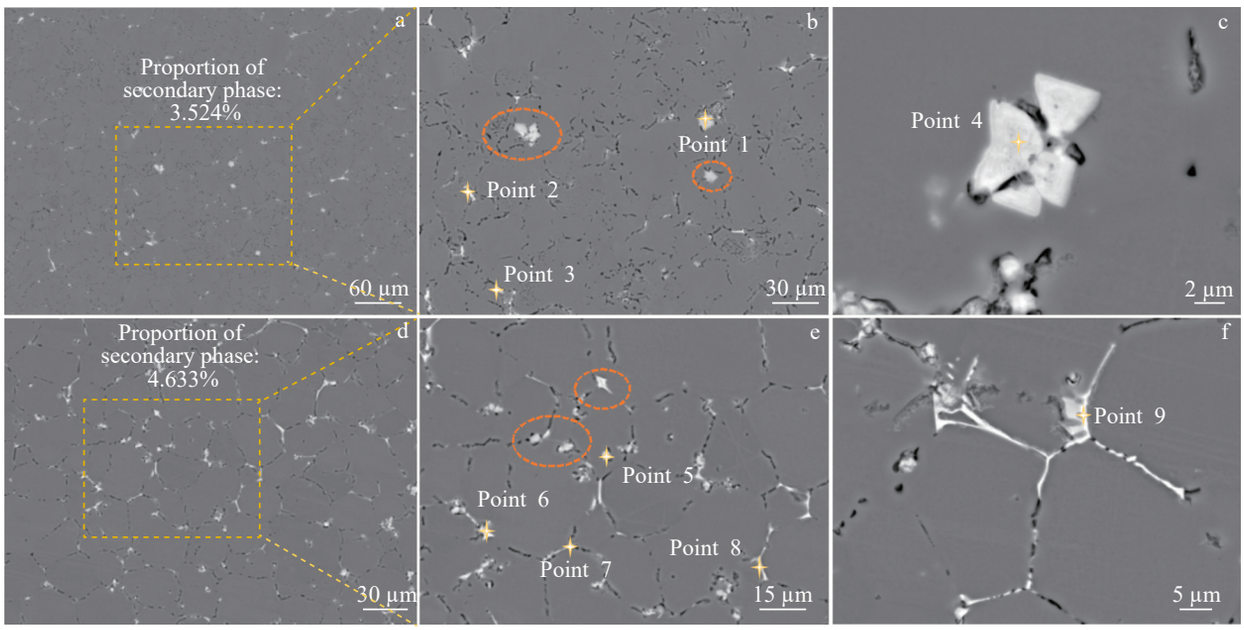

Fig.5 SEM microstructures of precipitation phases in as-cast Base alloy (a–c) and 0.1Y alloy (d–f)

Table 2 Element contents and possible intermetallic compounds of points marked in Fig.5 (at%)

Point	Al	Cu	Mg	Zr	Sc	Y	Intermetallic compound
1	82.35	1.82	0.18	10.14	5.51	-	Al_3(Sc, Zr)
2	52.97	47.03	-	-	-	-	Al_2CuLi
3	57.79	40.81	-	-	-	-	Al_2CuLi
4	86.61	-	-	5.07	8.33	-	Al_3(Sc, Zr)
5	82.48	-	-	13.22	4.29	-	Al_3(Sc, Zr)
6	91.16	8.24	-	-	-	0.6	Al_8CuY
7	87.81	12.28	-	-	-	-	Al_6CuLi_3
8	78.78	18.39	-	-	-	2.82	Al_8Cu_4Y
9	65.45	30.28	-	-	-	4.27	Al_8Cu_4Y

element Mg is uniformly distributed inside the grain. The elements Zr and Sc are distributed in the interior of the grains in a discrete manner, which generates the Al_3X (X=Zr, Sc, Li) incipient phase. According to Fig. 6d, it can be seen that the element Y in the 0.1Y alloy is uniformly distributed inside the matrix, and the addition of trace Y further promotes the segregation of Cu, forming a continuous band-like structure near the grain boundaries. The reason may be that the equilibrium partition coefficient of Y is much less than 1, leading to the formation of a solute boundary layer at the solidification front during solidification. The presence of Y atoms hinders the diffusion of Cu atoms across the solute boundary layer to both sides, reducing the effective partition coefficient of Cu. As a result, the number of Cu atoms dissolving in the α-Al matrix decreases, significantly increasing the volume fraction of secondary phases formed at the grain boundaries[23].

3.2 Microstructure analysis of heat-treated alloys

According to Fig. 4 and Fig. 5, element segregation and coarse intermetallic secondary phases can be observed at the grain boundaries of the as-cast alloy. These coarse secondary phases can disrupt the continuity of the Al-Li alloy matrix. When the alloy is subjected to external forces, the interfaces between these secondary phase particles and the matrix tend to become the stress concentration sources, facilitating the crack initiation and propagation at these locations, which is highly detrimental to the strength and plasticity of alloys. Therefore, appropriate heat treatment is necessary to eliminate these secondary phases and to mitigate their adverse effects. Through rapid cooling methods, such as quenching, a large number of solute atoms are retained in the α-Al matrix after solution treatment, forming a supersaturated solid solution, which lays a good foundation for subsequent aging[10].

To maximize the dissolution degree of secondary phases at grain boundaries while preventing the incipient melting of certain secondary phases, a two-stage solution treatment approach was adopted[24]. Considering the presence of multiple low-melting-point secondary phases, such as δ' (Al_3Li) and T_1 (Al_2CuLi) phases, in the matrix and grain boundaries of the Base and 0.1Y alloys, 480 °C was selected as the first-stage

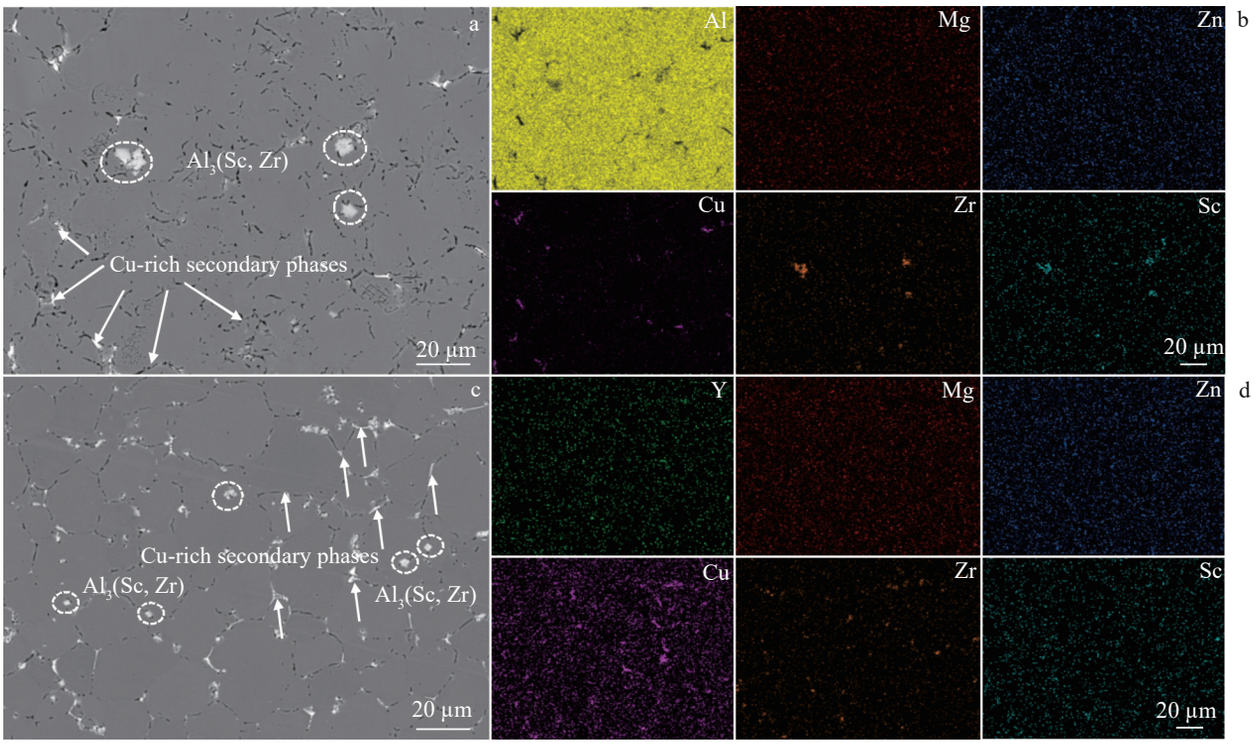

Fig.6 SEM images (a, c) and corresponding EDS element distributions (b, d) of as-cast Base alloy (a–b) and 0.1Y alloy (c–d)

solution treatment temperature[25]. However, this temperature is insufficient for the complete dissolution of all Cu-containing secondary phases. Therefore, a relatively higher temperature of 530 °C was selected for the second-stage solution treatment to further reduce the number of secondary phases at grain boundaries and to enhance the supersaturation of solutes in the alloy[26].

SEM and EDS analyses were conducted on the Base and 0.1Y alloys after solution treatment. As shown in Fig. 7a–7c, after solution treatment, most of the secondary phases at grain boundaries in both alloys dissolve into the matrix. A small portion of secondary phases remaining at the grain boundaries are also transformed from the as-cast continuous strip-like and network-like ones into discontinuous dot-like ones. The 0.1Y alloy exhibits a higher volume fraction of residual secondary phases.

Fig.7b and 7d show the distribution of elements in the Base and 0.1Y alloys after solution treatment, respectively. The results show that the distribution of Zn in the Base alloy after solid solution treatment is basically the same as that in the as-cast Base alloy. Zn is uniformly distributed in the matrix without element agglomeration. Mg completely dissolves in the matrix, and the presence of Mg cannot be observed at the grain boundaries. Cu shows the most obvious element segregation at the grain boundaries in the as-cast Base alloy. Most Cu enters the matrix after solid solution treatment, and only a small part of Cu remains at the grain boundaries. Zr and Sc remain within the grains, unaffected by the solution treatment. This is because the primary $Al_3(Sc, Zr)$ phase has a higher melting point than the matrix does, leading to less effect on the precipitation or dissolution by solution treatment. In the solution-treated 0.1Y alloy, due to the addition of Y, the number of residual secondary phases at the grain boundaries is greater than that in the solution-treated Base alloy. As shown in Fig. 7b, elements Cu, Zr, and Sc can be clearly detected.

The temperature of 175 °C, which is close to the solvus line of metastable Al_3Li in the Al-Li system, was chosen as the aging temperature[27]. Subsequently, the microstructures of the aged Base and 0.1Y alloys were analyzed using SEM. Fig. 8a–8c show SEM microstructures of the Base alloy after aging treatment. It can be seen that the grain size of the aged Base alloy shows a slight increase compared with that of the as-cast Base alloy, but no abnormal grain growth can be observed. The secondary phase with continuous stripe-like distribution is reprecipitated at the grain boundaries, and its precipitation amount is gradually increased with the prolongation of aging time. Fig. 8d–8f show SEM microstructures of the 0.1Y alloy after aging treatment. Compared with the aged Base alloy, the aged 0.1Y alloy has a larger number of secondary phases precipitated in the matrix. This phenomenon is consistent with that in the as-cast alloys. After aging, the grain size of both alloys has a certain reduction compared with that after solid solution treatment, but the reduction trend is not significant. The area fractions of the secondary phases at the grain boundaries of the Base and 0.1Y alloys after aging were analyzed, and the results are shown in Table 3. The area fractions of the secondary phases in the Base alloy are 1.57%, 1.77%, and 1.85% after aging for 8, 10, and 14 h, respectively. The area fractions of the secondary phases in the 0.1Y alloy

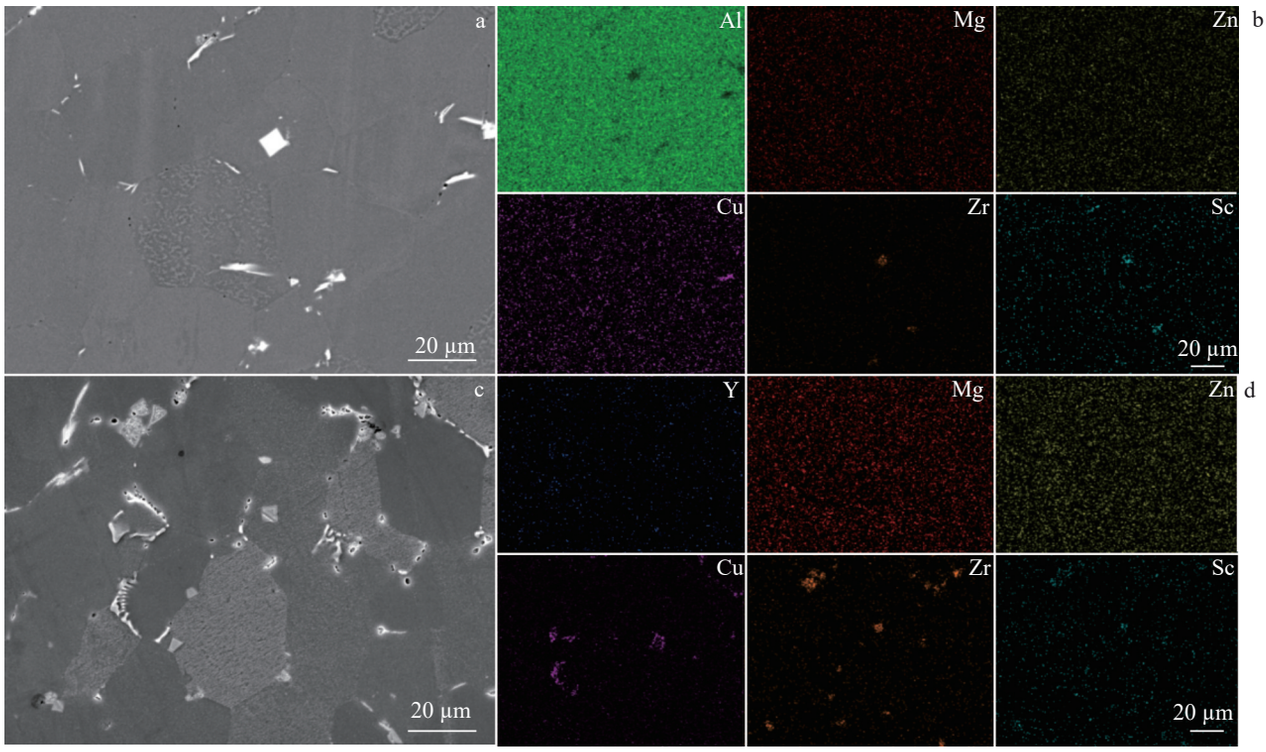

Fig.7 SEM images (a, c) and corresponding EDS element distributions (b, d) of Base alloy (a–b) and 0.1Y alloy (c–d) after solid solution treatment

are 2.74%, 2.86%, and 2.94% after aging for 8, 10, and 14 h, respectively. This result indicates that the element Y can also promote the precipitation of secondary phases in the Base alloy after aging treatment.

3.3 Analysis of mechanical properties after heat treatment

Tensile tests were conducted on the Base and 0.1Y alloys after solid solution treatment and subsequent aging for 8, 10, and 14 h, and the results are shown in Fig. 9. From Fig. 9a, it can be directly observed that the ultimate tensile strength, yield strength, and elongation of the Base alloy after solid solution treatment are 244 MPa, 145 MPa, and 6.4%, respectively. The ultimate tensile strength, yield strength, and elongation of the 0.1Y alloy after solution treatment are 290 MPa, 148 MPa, and 11.8%, respectively. Compared with the

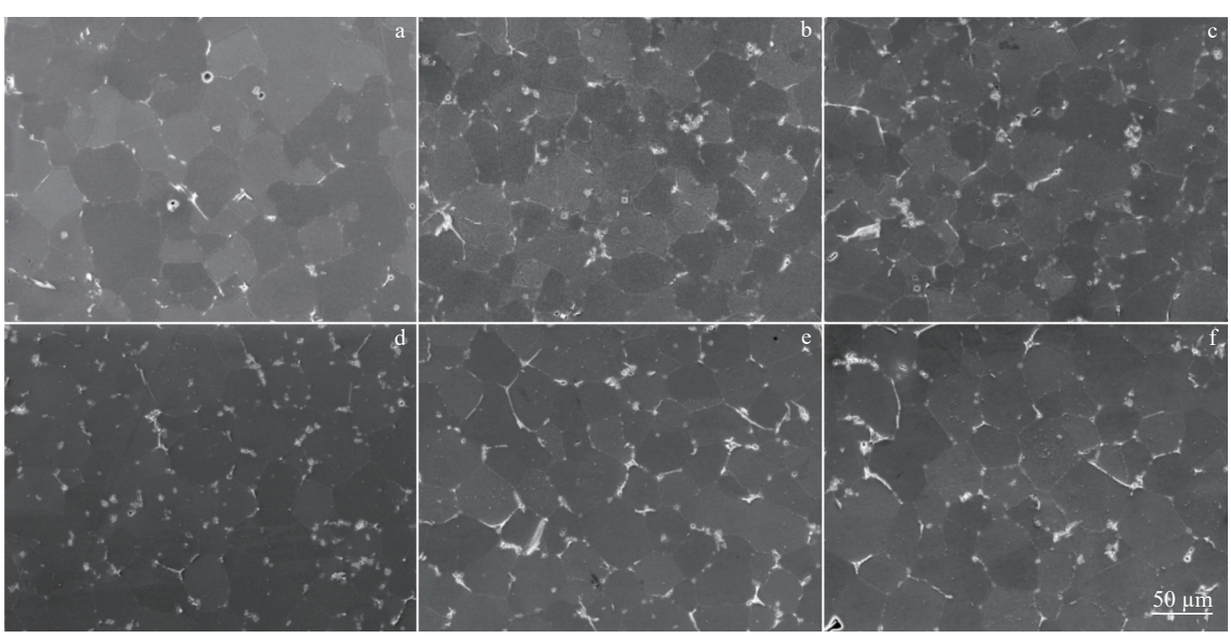

Fig.8 SEM microstructures of Base alloy (a–c) and 0.1Y alloy (d–f) after solid solution and subsequent aging treatment for 8 h (a, d), 10 h (b, e), and 14 h (c, f)

Table 3 Area fraction of the secondary phases at grain boundaries of Base and 0.1Y alloys after solid solution+ aging treatment for different durations

Alloy	Area fraction of secondary phases/%		
	8 h	10 h	14 h
Base	1.57	1.77	1.85
0.1Y	2.74	2.86	2.94

solution-treated Base alloy, the solution-treated 0.1Y alloy exhibits 18.9% increase in ultimate tensile strength and 84.4% increase in elongation. A pronounced Portevin-Le Chatelier (PLC) effect can be observed in the tensile curves after solution treatment[28–29], as shown in Fig. 9. This plastic instability phenomenon is mainly related to the interaction between Cu and Li solute atoms and the movement of dislocations, which also implies that the content of solute atoms in the alloy matrix is at a high level, indicating good plasticity.

With the prolongation of aging time, the overall strength of the alloy shows a trend of firstly increase and then decrease. As shown in Fig.9a, the ultimate tensile strength of the Base alloy after aging at 175 °C for 8, 10, and 14 h is 355, 359, and 330 MPa, and the elongation is 3.0%, 4.1%, and 2.4%, respectively. The ultimate tensile strength of the 0.1Y alloy after aging at 175 °C for 8, 10, and 14 h is 398, 412, and 384 MPa, and the elongation is 4.1%, 6.3% and 4.3%, respectively. The mechanical properties of the Base and 0.1Y alloys after aging for 10 h show the optimal combination. The increase in strength is mainly due to the evolution of the T_1, S′, and δ' phases during the artificial aging process[30]. Compared with that at the solid solution state, the ultimate tensile strength of Base alloy after aging for 10 h increases by 45% and the elongation decreases by 35%. Compared with that at the solid solution state, the ultimate tensile strength of 0.1Y alloy after aging for 10 h increases by 48% and the elongation decreases by 45%. The ultimate tensile strength and elongation of 0.1Y alloy aged for 10 h increase by about 16.1% and 53.7%, respectively, compared with those of Base alloy aged for 10 h.

The overall results indicate that the 0.1Y alloy after aging treatment has superior mechanical properties.

To better understand the variations in the mechanical properties of the Base and 0.1Y alloys after heat treatment, the fracture morphologies were analyzed. As shown in Fig. 10, the Base and 0.1Y alloys exhibit almost identical fracture characteristics under the same conditions. From Fig.10a and 10e, it is clear that the fracture surfaces of both alloys after solid solution treatment are covered with dimples of varying depths and sizes, and the secondary phase particles are at the bottom of the dimples, which is a typical toughness fracture characteristic caused by the growth and aggregation of micropores. As shown in Fig.10b and 10f, the proportion of deep dimples in the solid-solution-treated 0.1Y alloy is significantly higher than in the solid-solution-treated Base alloy. More deep dimples are beneficial to plasticity enhancement. After aging treatment, the fracture characteristics of the alloys undergo significant changes from the tough fracture to the brittle fracture with the “rock candy” fracture morphology, as shown in Fig.10c and 10g. After aging for 10 h, the fracture modes of both alloys are primarily quasi-cleavage and partial intergranular fracture with the fracture surfaces consisting mainly of tear ridges and showing numerous smooth facets, as shown in Fig. 10d and 10h. Additionally, there are also some broken particles at the grain boundaries, and it may be because the Cu-rich secondary phase continuously distributed at the grain boundaries is torn and broken during the tensile process and eventually falls off. Under the action of tensile stress, pores are generated in the secondary phase and continue to extend. Further decomposition and fragmentation of the secondary phase will continue to generate new pores. With the increase in the number of pores, fracture eventually occurs[27]. With the prolongation of aging duration, the dimples gradually become shallower or even disappear, which infers the decrease in elongation. According to Ref. [31], massive secondary precipitates can provide potential sites for the stress concentration and possible pathways for crack propagation. Therefore, the precipitation of secondary phases during aging is the main cause of plasticity degradation.

4 Discussion

4.1 Grain refinement mechanism of element Y

The Jmatpro simulation results show that the addition of

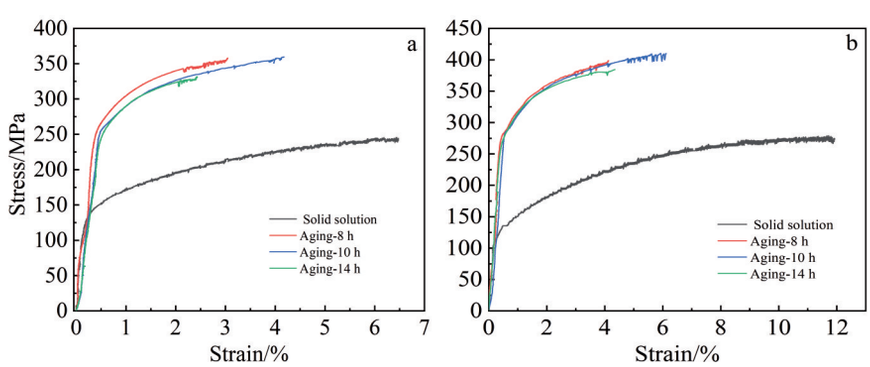

Fig.9 Stress-strain curves of Base alloy (a) and 0.1Y alloy (b) after solid solution and subsequent aging for different durations

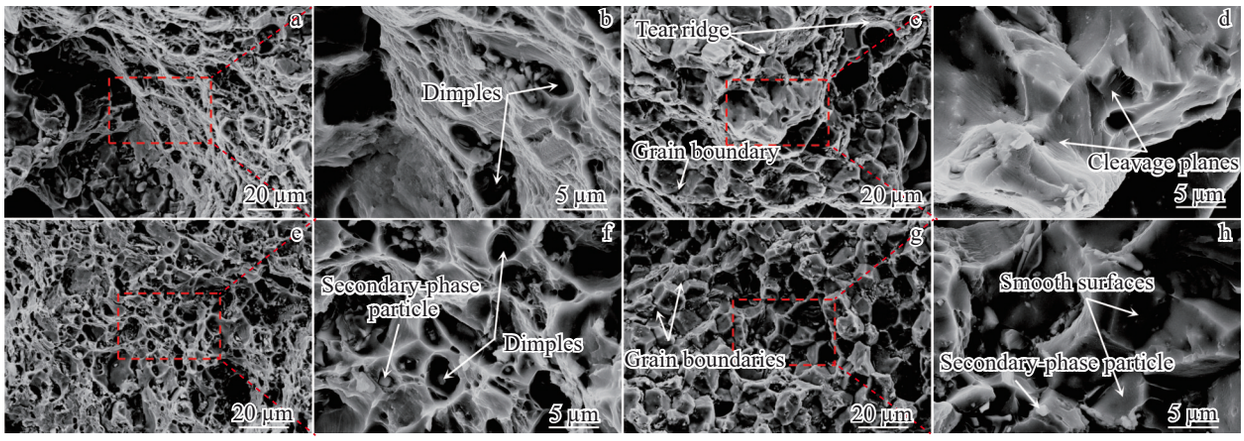

Fig.10 Tensile fracture surfaces of of Base alloy (a–d) and 0.1Y alloy (e–h) after solid solution (a–b, e–f) and subsequent aging treatment for 10 h (c–d, g–h)

0.1wt% Y significantly increases the precipitation temperature of the Al_3Sc and Al_3Zr phase, as shown in Fig.3. An increase in temperature accelerates the diffusion rate of atoms, which promotes the migration of solute atoms to the precipitated phase and facilitates the precipitation process. This result suggests that at higher temperatures, Al_3Zr and Al_3Sc phases will nucleate and crystallize, leading to easier precipitation in the matrix and thereby increasing the number of Al_3Sc and $Al_3(Sc, Zr)$ phases in the α-Al matrix. The formation of Al_3Sc intermetallic compounds during solidification occurs via three distinct mechanisms: (1) precipitation of primary Al_3Sc phase directly from the liquid phase in hypereutectic composition; (2) formation of Al+Al_3Sc eutectic microstructure through eutectic reaction; (3) precipitation of nanoscale Al_3Sc particles from Sc-supersaturated regions in the as-cast matrix[32].

Al_3Sc is an $L1_2$-type ordered equilibrium phase with a lattice constant of 0.4103 nm and it has the same lattice type as that of α-Al (0.405 nm)[27] with a lattice mismatch of only 1.32% with α-Al, showing high co-lattice properties. The lattice parameter of Al_3Zr is 0.4107 nm, which is fully coherent with the α-Al matrix with lattice mismatch of 1.634%. The activation energy for diffusion of Sc in α-Al matrix (173 kJ/mol) is significantly lower than that of Zr (242 kJ/mol). During non-equilibrium solidification, the primary Al_3Sc intermetallic phase nucleates preferentially within the α-Al matrix, followed by partial diffusion of Zr into Al_3Sc to form $Al_3(Sc, Zr)$ phase[33]. Then, the residual Al_3Sc is precipitated as dispersed Al_3Sc phase. Concurrently, the eutectic transformation ($L\rightarrow\alpha$-Al+Al_3Sc) proceeds during the solidification of the residual liquid phase. Due to the equilibrium partition coefficient of Sc (k=0.63<1), Sc enriches at the solid-liquid interface, ultimately forming irregularly-shaped eutectic Al_3Sc phase along grain boundaries from the residual liquid. Similarly, Zr diffuses into the eutectic Al_3Sc, ultimately producing the eutectic $Al_3(Sc, Zr)$ intermetallic phase. The $Al_3(Sc, Zr)$ phase is similarly co-lattice with the α-Al matrix.

The intermetallic phases $Al_3(Sc, Zr)$, Al_3Zr, and Al_3Sc exhibit negligible differences in lattice parameters (0.4103 – 0.4107 nm), maintain perfect coherency with the α-Al matrix, and have similar sizes, making them difficult to distinguish by conventional methods. Furthermore, the elevated interfacial energy of these precipitates (Al_3Zr/Al_3Sc) and the α-Al matrix results in the scarcity of isolated Al_3Zr or Al_3Sc phases[34]. Therefore, in Al-Li alloys containing both Sc and Zr, these precipitates are conventionally designated as the $Al_3(Sc, Zr)$ phase in most cases.

Meanwhile, Al_3Zr, Al_3Sc, and $Al_3(Sc, Zr)$ phases are discretely distributed within the grains, as shown in Fig.6a and 6c, and they can serve as effective heterogeneous nucleation sites[35–36], accelerating the α-Al crystallization rate and refining the grains. Qin et al[37] calculated the interfacial energies of Al/Al_3Sc, Al/Al_3Zr, and Al_3Sc/Al_3Zr interfaces with contact surfaces of (001)/(001), (110)/(110), and (111)/(111) by first-principles, respectively. The results show that among different contact surfaces, $Al_3(Sc, Zr)$ has the lowest interfacial energy and a stronger ability for heterogeneous nucleation. This result also suggests that the presence of more $Al_3(Sc, Zr)$ phases in the matrix is more beneficial to grain refinement in the alloy. As shown in Fig. 2c and 2f, the grain size of the alloy decreases from 29.81 μm to 18.56 μm after the addition of 0.1wt% Y.

The role of element Y in grain refinement is multifaceted. In addition, the grain size refinement is also related to the behavior characteristics of Y during solidification. Firstly, the rare earth Y is usually excluded from the solidified phase during solidification, accumulating in the liquid phase ahead of the solid-liquid interface, which leads to increased concentration fluctuations at the interface, enhances the undercooling of the alloy during solidification[19,38], and promotes the nucleation. With the continuous aggregation of trace element Y, an enriched layer is gradually formed along the solid-liquid interface, which hinders the advancement of the liquid-solid interface and the diffusion of Al and Cu atoms at the interface. The enrichment of element Y slows down the growth rate of the grains, which reduces the grain size

accordingly[23,39–40]. Secondly, the chemical properties of element Y are quite active[41], and the electronegativity of Y is 1.22, which is lower than that of Al (1.50). When Y dissolves in the aluminum melt, it can easily fill the defects on the surface of alloy phase, reduce the surface tension at the interface between the old and new phases, and increase the nucleation rate[42–43]. Finally, the addition of element Y increases the distortion of the lattice and raises the system energy. To maintain the lowest free energy of the system, Y migrates to the grain boundaries and combines with other elements to form complex compounds. These compounds are segregated at the grain boundaries, which also hinders the continuous growth of α-Al, thus refining the grains.

4.2 Contribution of element Y to mechanical property enhancement

It is reported that the addition of element Y significantly improves the mechanical properties of the alloys, resulting in a significant increase in both strength and plasticity. The aging-treated 0.1Y alloy has a finer grain size and more secondary precipitated phases, compared with the Base alloy. In this case, it can be assumed that the improvement in mechanical properties of 0.1Y alloy is mainly attributed to secondary-phase strengthening and fine-grain strengthening, and the fine-grain strengthening is the most important type of strengthening mechanisms.

The addition of Y significantly refines the grains, and the contribution of grain refinement can be quantified according to the Hall-Petch formula[44]:

$$\Delta\sigma_{\text{grain}} = k\left(d_1^{-1/2} - d_2^{-1/2}\right) \quad (1)$$

where $\Delta\sigma_{\text{grain}}$, k, d_1, and d_2 represent the increase in tensile strength after grain refinement, the Hall-Petch constant, the refined grain size, and the original grain size, respectively. From Eq. (1), the tensile strength is increased with the decrease in grain size. According to the Hall-Petch relationship, a smaller average grain size means more grain boundaries, and the increase in grain boundaries enhances the resistance against dislocation movement. When dislocations move from the grain interior to the grain boundaries, these dislocations are hindered by the grain boundaries, resulting in the formation of dislocation stacking. If the deformation continues, the external force must be increased, which further increases the material strength[45]. Due to the presence of Y-containing intermetallic compounds in the matrix, the dislocation ring remains when the dislocations bypass the precipitates, realizing dislocation multiplication and thus increasing the alloy strength[42]. Meanwhile, fine grains indicate more grains per unit volume, which means that the same amount deformation can be carried by more grains. Therefore, the deformation generated by external force can be uniformly dispersed to more grains, which avoids localized stress concentration and crack formation, and significantly improves the plasticity of the alloy. Based on the above analysis, the grain refinement induced by element Y plays a crucial role in improving both the strength and plasticity of the alloy.

Secondary-phase strengthening is also an important mechanism to enhance the mechanical properties of Al-Li alloys. The type, quantity, and size of secondary phases all play vital roles in modifying the mechanical properties. Comparison between Base and 0.1Y alloys shows that with 0.1wt% Y addition, the tensile strength of 0.1Y alloy increases by about 16%, compared with that of the Base alloy, as shown in Fig.9b. According to Fig.11a and 11d, the δ' phase size in the Base alloy is about 20 nm, whereas it is about 18 nm in the 0.1Y alloy. Comparatively, the δ' size in the 0.1Y alloy shows a slight decrease. Fig.11b–11c show uniformly distributed fine δ' phases in the Base alloy matrix, along with core-shell structured nanoscale Al_3(Li, Sc, Zr) phases. Fig.11e–11f show the microstructure, quantity, and size of δ' and Al_3(Li, Sc, Zr) phases in 0.1Y alloy. Comparison reveals that δ' phases in 0.1Y alloy are more numerous, densely distributed, and finer in size. More notably, Al_3(Li, Sc, Zr) phases show a dramatic increase in quantity with slight coarsening. These phenomena further confirm that Y addition promotes massive precipitation of these composite phases.

The secondary-phase strengthening mechanism in the 0.1Y alloy primarily originates from two distinct aspects[26,34]: the precipitation of fine-scale δ' phases and the formation of abundant Sc/Zr-enriched Al_3(Li, Sc, Zr) precipitates with core-shell morphology, as demonstrated in Fig.11.

In Al-Li alloy systems, δ' precipitates remarkably enhance the mechanical performance via multiple synergistic strengthening mechanisms. Characterized by an $L1_2$ ordered crystal structure, the δ' precipitates provide strengthening effect through the combined influence: (1) precipitation strengthening; (2) coherency strain reinforcement; (3) order strengthening[46]. The precipitation strengthening effect is primarily attributed to nanoscale δ' precipitates (typically 10–50 nm in diameter) with homogeneous dispersion, which serve as potent barriers against dislocation glide. Dislocations must bypass (via Orowan mechanism) or cut through the precipitates. When the Orowan mechanism dominates, the critical resolved shear stress is increased significantly with the decrease in interparticle spacing, thereby enhancing the yield strength. A minimal lattice misfit of approximately 0.08% between δ' precipitates and the α-Al matrix generates coherent strain fields surrounding each particle, further impeding the dislocation slip. The $L1_2$-ordered structure of δ' precipitates necessitates the formation of anti-phase boundaries when dislocations shear through them, demanding considerable energy to disrupt the long-range atomic ordering. The volume fraction and size of δ' phase directly affect strengthening effect: nanoscale particles (<30 nm) with high volume fraction (>10%) provide maximum strengthening effect.

The strengthening effect of Al_3(Sc, Zr) phase is mainly reflected in the Orowan dislocation bypass mechanism. Specifically, mobile dislocations bypass non-shearable Al_3(Sc, Zr) particles, forming dislocation loops around them and achieving the dislocation multiplication[50]. The increased critical resolved shear stress required for remaining dislocations to bypass particles and to continue moving

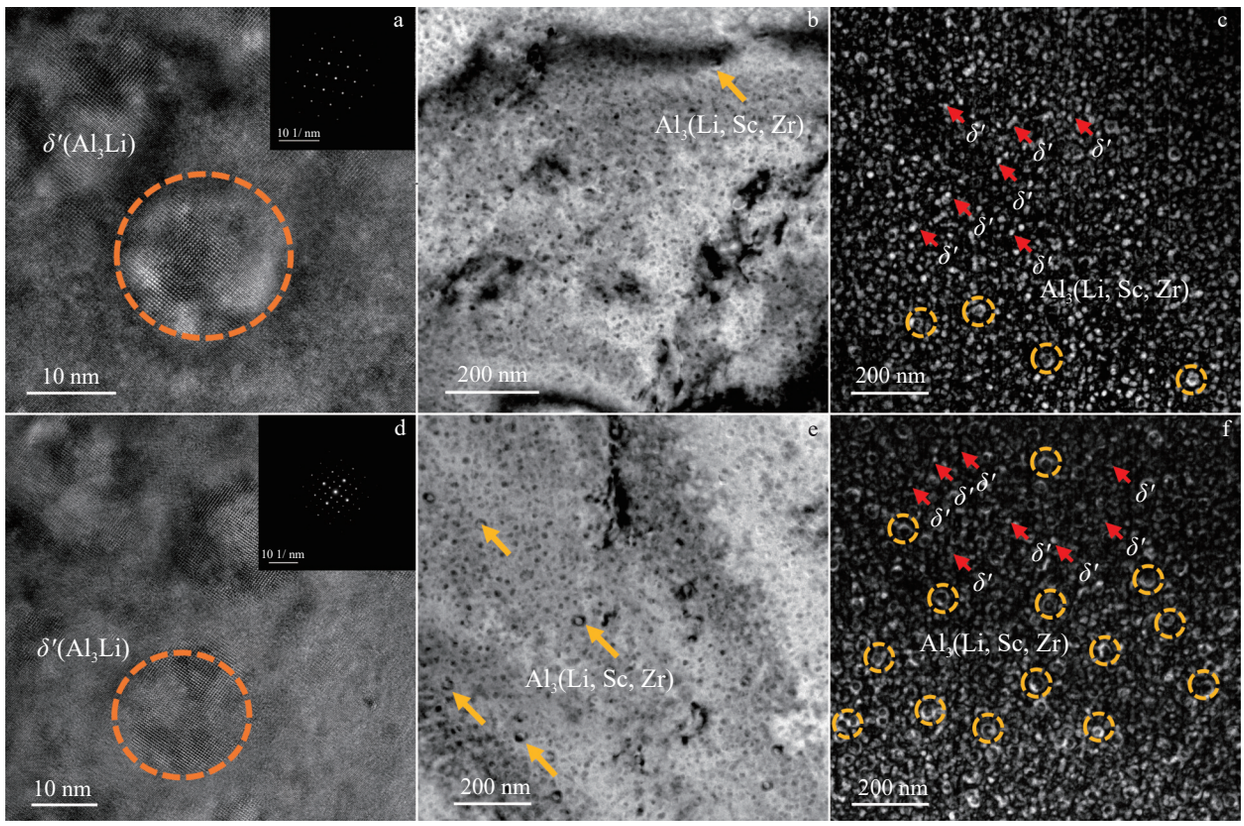

Fig.11 TEM analyses of Base alloy (a–c) and 0.1Y alloy (d–f) after solid solution and subsequent aging for 10 h: (a, d) high resolution TEM images of Al_3Li particles and corresponding SAED patterns along $[001]_{Al}$ zone axis; (b, e) bright-field images of Al_3Li particles; (c, f) dark-field images of Al_3Li particles

enhances the alloy strength. Moreover, $Al_3(Sc, Zr)$ particles exhibit low coarsening rates[47] while simultaneously acting as potent heterogeneous nucleation sites for δ' precipitates in the Al-Li alloy. Leading to the formation of non-shearable $Al_3(Li, Sc, Zr)$ composite phases to further enhance Orowan strengthening[48]. The increased volume fraction of $Al_3(Li, Sc, Zr)$ particles and significant grain refinement are the main reasons for the remarkable improvement in strength and ductility of 0.1Y alloy, as shown in Fig. 9b. Radmilovic et al[49] indicated that Li increases the nucleation driving force for Al_3Sc by reducing Sc solubility in α-Al matrix, thereby enhancing Sc supersaturation. In this research, the greater number of $Al_3(Li, Sc, Zr)$ in the 0.1Y alloy matrix improves the mechanical properties. The evolution of $Al_3(Sc, Zr)$ phase during aging process largely determines the mechanical properties of Al-Li alloys[51].

5 Conclusions

1) The addition of Y has a significant refinement effect on the grains of Al-2.2Li-1.5Cu-0.5Mg-1Zn-0.2Zr-0.2Sc alloy: the grain size reduces from 29.81 μm to 18.56 μm. The refinement mechanism mainly includes the promotion of Al_3Sc and $Al_3(Sc, Zr)$ precipitation by Y addition, leading to the increase in heterogeneous nucleation sites and the hindrance of solid-liquid interface migration by Y-containing Cu-rich secondary phases.

2) After solid solution treatment, most of the copper-rich secondary phases intermittently distributed at the grain boundaries in the as-cast organization of 0.1Y alloy are dissolved in the matrix, and the grains do not grow abnormally. After subsequent aging treatment, a small number of secondary phases are reprecipitated at the grain boundaries. The tensile strength of aged 0.1Y alloy reaches 412 MPa, and plasticity is 6.3% after aging at 175 °C for 10 h. The excellent mechanical properties are attributed to the fine-grain strengthening effect of the element Y and the presence of secondary strengthening phases precipitated in the aging process.

3) The presence of dimples can be observed in the fracture of both alloys after solid solution treatment. Meanwhile, the 0.1Y alloy has a higher number and denser distribution of dimples, indicating better plasticity. The fracture mode of both Base and 0.1Y alloys after aging treatment changes from ductile fracture (solid-solution state) to brittle fracture dominated by quasi-cleavage fracture and partial intergranular fracture (aging state). This is because the secondary phases reprecipitated during the aging process provide favorable conditions for the extension of microcracks.

References

1 Yu X X, Yin D F, Yu Z M *et al. Rare Metal Materials and Engineering*[J], 2016, 45(7): 1687

2 Shao L X, Li X F, Sun G Q *et al. Journal of Materials Research and Technology*[J], 2024, 28: 4710

3 Zhang X L, Zhang L, Wu G H *et al. Materials Characterization*[J], 2017, 132: 312

4 Araullo-Peters V, Gault B, Geuser F D *et al. Acta Materialia*[J], 2014, 66: 199

5 Li H Y, Huang D S, Kang W *et al. Journal of Materials Science & Technology*[J], 2016, 32(10): 1049

6 Liu Y, Zhao C X, Chen J F *et al. Journal of Materials Research and Technology*[J], 2024, 30: 2728

7 Duan S W, Matsuda K, Wang T *et al. Rare Metals*[J], 2021, 40(7): 1897

8 Chen S K, Jin Y J, Wei H *et al. Applied Surface Science*[J], 2025, 680: 161334

9 Zhang S, Qi F Z, Zhang L *et al. Materials Science and Engineering A*[J], 2024, 896: 146300

10 Duan S W, Liu Z L, Guo F Q *et al. Journal of Materials Research and Technology*[J], 2023, 22: 2502

11 Zhang J S, Wu G H, Zhang L *et al. Journal of Materials Science & Technology*[J], 2022, 96: 212

12 Deng Y L, Xu J J, Chen J Q *et al. Materials Science and Engineering A*[J], 2020, 795: 139975

13 Xue C P, Wang J S, Yang X H *et al. Applied Materials Today*[J], 2024, 38: 102176

14 Zhang X L, Zhang L, Wu G H *et al. Materials Characterization*[J], 2018, 142: 223

15 Wang Y, Li Z, Yu T F *et al. Advanced Engineering Materials*[J], 2018, 20(4): 1700898

16 Zhang X L, Wu G H, Zhang L *et al. Journal of Alloys and Compounds*[J], 2019, 788: 367

17 Zhang X J, Wang H W, Yan B *et al. Materials Science and Engineering A*[J], 2021, 822: 141641

18 Zhang Y Z, Gu J, Tian Y *et al. Materials Science and Engineering A*[J], 2014, 616: 13

19 Li H Z, Liang X P, Li F F *et al. Transactions of Nonferrous Metals Society of China*[J], 2007, 17(6): 1194

20 Xu J J, Deng Y H, Chen J Q *et al. Materials Science and Engineering A*[J], 2020, 773: 138885

21 Wang Y X, Wu G H, Zhang L *et al. Materials Science and Engineering A*[J], 2023, 880: 145366

22 Ji H, Peng X, Zhang X L *et al. Journal of Alloys and Compounds*[J], 2019, 791: 655

23 Deng A L, Chen H, Zhang Y B *et al. Materials Science and Engineering A*[J], 2024, 892: 146101

24 Fu R, Huang Y C, Liu Y *et al. Transactions of Nonferrous Metals Society of China*[J], 2023, 33(8): 2255

25 Wu L, Li X F, Wang H W. *Materials Characterization*[J], 2021, 171: 110800

26 Zhang J S, Zhong X X, Zhang L *et al. Transactions of Nonferrous Metals Society of China*[J], 2022, 32(2): 411

27 Shi C C, Zhang L, Wu G H *et al. Materials Science and Engineering A*[J], 2017, 680: 232

28 Qi F Z, Wu G H, Zhang L *et al. Journal of Materials Science & Technology*[J], 2024, 199: 1

29 Wu C H, Li H, Bian T J *et al. Materials Characterization*[J], 2022, 184: 111694

30 Xue C P, Wang S, Wang J S *et al. Nano Letters*[J], 2025, 25(11): 4636

31 Peng Y, Chen A, Zhang L *et al. Journal of Materials Research*[J], 2016, 31(8): 1124

32 Marquis E A, Seidman D N. *Acta Materialia*[J], 2001, 49(11): 1909

33 Tolley A, Radmilovic V, Dahmen U. *Scripta Materialia*[J], 2005, 52(7): 621

34 Xue C P, Wang S, Zhang Y X *et al. Materials Science and Engineering A*[J], 2023, 881: 145393

35 Shi C C, Wu G H, Zhang L *et al. Journal of Alloys and Compounds*[J], 2021, 885: 161106

36 Jiang B, Yi D Q, Yi X O *et al. Materials Characterization*[J], 2018, 141: 248

37 Qin J, Tan P, Quan X *et al. Journal of Alloys and Compounds*[J], 2022, 909: 164686

38 Wang Z C, Zhang C M, Li S L *et al. Journal of Materials Research and Technology*[J], 2024, 33: 5518

39 Chen Y F, Zhu Z Q, Zhou J X. *Materials Science and Engineering A*[J], 2022, 850: 143513

40 Ding W W, Zhao X Y, Chen T L *et al. Journal of Alloys and Compounds*[J], 2020, 830: 154685

41 Li J H, Zhang Y B, Li M J *et al. Materials & Design*[J], 2022, 223: 111129

42 Ding X X, Lu Y L, Wang J *et al. Metals*[J], 2023, 13(2): 253

43 Zhang X G, Mei F Q, Zhang H Y *et al. Materials Science and Engineering A*[J], 2012, 552: 230

44 Qian W, Zhao Y T, Kai X Z *et al. Journal of Alloys and Compounds*[J], 2020, 829: 154624

45 Li A M, Wang L Z, Hu Y *et al. Journal of Physics: Conference Series*[J], 2021, 2044: 012070

46 Radmilovic V, Tolley A, Marquis E A *et al. Scripta Materialia*[J], 2008, 58(7): 529

47 Bogno A A, Henein H, Ivey D G *et al. Canadian Metallurgical Quarterly*[J], 2020, 59(1): 101

48 Yang C, Zhang P, Shao D *et al. Acta Materialia*[J], 2016, 119: 68

49 Radmilovic V, Ophus C, Marquis E A *et al. Nature Materials*[J], 2011, 10(9): 710

50 Shun E, Deng J C, Wang H N *et al. Rare Metal Materials and Engineering*[J], 2023, 52(6): 2048

51 Cui X M, Liang S B, Zhao X P *et al. Rare Metal Materials and Engineering*[J], 2023, 52(5): 1603

Y元素对铸造Al-2.2Li-1.5Cu合金晶粒细化和力学性能的影响

王　旭[1]，党　乾[1]，马鸿耀[1]，刘国怀[1]，张　弛[2]，王昭东[1,3]

(1. 东北大学 数字钢铁全国重点实验室，辽宁 沈阳 110819)

(2. 沈阳工业大学 材料科学与工程学院，辽宁 沈阳 110870)

(3. 河南省科学研究院 材料研究所，河南 郑州 450046)

摘　要：探究了微量0.1wt%Y元素的加入对于铸造Al-2.2Li-1.5Cu-0.5Mg-1Zn-0.2Zr-0.2Sc合金在铸态及热处理态下晶粒细化和力学性能的影响。结果表明：添加0.1wt% Y元素到Al-2.2Li-1.5Cu-0.5Mg-1Zn-0.2Zr-0.2Sc合金中，能够提升Al_3(Sc, Zr)相的形核温度，导致Al_3(Sc, Zr)相优先析出，增加了其在基体中的分布数量。并且，Al_3(Sc, Zr)相作为α-Al基体中的非均质形核位点，能够加速形核，细化晶粒。Y元素的加入改变了铸态合金晶界处的析出相特征，使得初始在晶界呈连续粗大条状分布的第二相转变为了断续点状、棒状分布，并且尺寸更小、数量更多。在细晶强化和沉淀强化的共同作用下，经过175 ℃/10 h时效处理后Al-2.2Li-1.5Cu-0.5Mg-1Zn-0.2Zr-0.2Sc-0.1Y合金极限抗拉伸强度达到了412 MPa，延伸率为6.3%，相较于未加入Y元素的合金抗拉伸强度和延伸率分别提高了16.1%和53.7%。

关键词：Al-Li合金；Y元素；热处理；晶粒细化

作者简介：王 旭，男，2000年生，硕士生，东北大学数字钢铁全国重点实验室，辽宁 沈阳 110819，E-mail：2270566@stu.neu.edu.cn